

Influence of Metallurgy on the Protective Mechanism of Chromium-Based Conversion Coatings on Aluminum–Copper Alloys

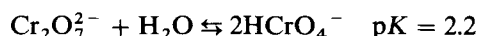
Patrick L. Hagans† and Christina M. Haas*

Henkel Corporation, Research and Development, 300 Brookside Avenue, Ambler, PA 19002, USA

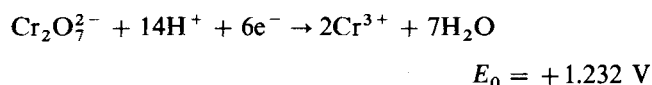
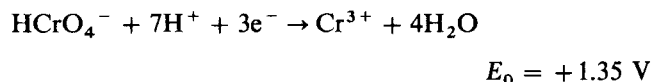
Several important aspects relating to the mechanism of formation of protective Cr-based oxide films on aluminum alloy 2024-T3 generated from CrO_3 + NaF-containing solutions were observed with electrochemical, AES and XPS measurements. Although the film deposition rate and surface composition were very much influenced by the presence of both Fe- and Cu-containing intermetallic phases, a uniform composition and thickness was eventually reached with increased coating time. This behavior is believed to be responsible for obtaining corrosion-resistant films on such heterogeneous surfaces. Surface Cr was consistently found to be in both the 3+ and 6+ oxidation states in an approximately 40 : 60 ratio, respectively, if x-ray beam reduction of Cr(VI) was accounted for. The enriched Cu layer found on the surface of polished 2024-T3 was found to remain intact during Cr–O film formation. The presence of Cr(VI) provides a ‘self-healing’ aspect to the film’s protective mechanism by remaining available for reduction to Cr(III) during oxidative attack. Addition of potassium ferro- or ferricyanide to the bath resulted in a film which obtained Fe, C and N enriched at the surface on both the matrix and intermetallic regions. These constituents were found, however, to be enriched and distributed throughout the entire depth of the film on the high Cu-bearing intermetallic regions, suggesting that the formation of a Cu–ferrocyanide complex is responsible for the benefit derived from these compounds.

INTRODUCTION

Immersion of Al and Al alloys into acidic (pH 1) baths containing chromic acid (CrO_3) + NaF produces a thick, extremely corrosion-resistant film composed of hydrated Cr(III) oxide and Al(III) oxide.¹ The alloy surfaces are usually cleaned and deoxidized before immersion, resulting in a thin (~ 50 Å) oxide overlayer. Known as a conversion coating because it contains both substrate and depositing species, Cr oxide/Al oxide film growth is assumed to proceed via redox chemistry. At low pH, CrO_3 exists in solution as either HCrO_4^- or $\text{Cr}_2\text{O}_7^{2-}$

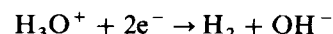


Both of these species are excellent oxidizing agents, as indicated by their large, positive reduction potentials



Aluminum is easily oxidized by either of these species. Both Al(III) and Cr(III) react with water or surface

hydroxyl ions formed by the reduction reaction



to form a surface layer composed of a mixture of Cr and Al hydroxides or oxyhydroxides. As the film is highly hydrated and amorphous, it is unlikely that the composition has a discrete stoichiometry.

The presence of F^- is important for building films of significant thickness; without its presence, film growth is extremely slow. Fluoride probably serves two roles: first, it solubilizes the Al oxide initially present on the surface and allows the deposition reactions to proceed. Secondly, F^- can also solubilize a portion of the growing film, which would allow penetration of the electrolyte to the surface and ion transport from the surface into the growing film. Fluoride has been characterized as a unique monodentate ligand which enhances the dissolution rate of Al oxide.²

In addition to CrO_3 + NaF, $\text{K}_3\text{Fe}(\text{CN})_6$ is often added to chromating baths where the greatest corrosion resistance is required.^{1,3,4} Examples include Cu-containing Al alloys such as 7075-T6 and 2024-T3, often used in the aerospace industry. Ferricyanide has to be termed a coating ‘accelerator’ since the coating weight is generally enhanced by its presence.¹ It is not clear from the literature, however, whether this applies to pure Al and all Al alloys. The mechanism by which ferricyanide enhances the corrosion resistance of these coatings is not known but some suggestions have been proposed.^{1,4}

Given the strong environmental concerns associated with most of the components of chromating baths (i.e. hexavalent Cr,^{5,6} HF and cyanide), a strong need to

* Author to whom correspondence should be addressed.

† Current address: Naval Research Laboratory, Code 6170, Washington, DC 20375, USA.

obtain alternative, more environmentally friendly treatments exists. One approach to discovering alternative chemistries is to understand in detail the mechanism of film formation and why the film renders the surface corrosion-resistant. A number of studies involving microscopy,⁷⁻¹⁰ SIMS,¹⁰⁻¹² XPS,^{3,4,10,12,13} AES^{10,12} and XANES (x-ray absorption near-edge spectroscopy)¹⁴ have been used to study film formation; however, the bulk of these studies have been conducted on pure Al rather than technologically relevant Al alloys. Some alloy work has been reported¹⁴ but surface probes sensitive to detection of second-phase precipitates or intermetallics and their influence on film growth were not utilized. This work was undertaken to determine the influence of alloy metallurgy on the formation of Cr-based conversion coatings. Specifically, the influence of Cu- and Fe-containing intermetallics on the formation of Cr-based conversion coatings has been examined with electrochemical, AES and XPS measurements. In addition, the same techniques have been employed to elucidate the role of ferricyanide in the film-forming process.

EXPERIMENTAL

The 2024-T3 aluminum alloy samples were obtained from Metal Samples Co., Inc. (Munford, AL) as disks 1.90 cm in diameter and 0.32 cm thick. The bulk composition of the alloy was determined by atomic absorption and is shown in Table 1. Similar sized aluminum disks were cut from a rod of 99.999% purity obtained from Johnson-Matthey. All data were taken with surfaces in the highly polished state, which was accomplished in the following manner: samples were mounted in epoxy and mechanically polished with a Buehler automated polishing system (Automet 2 head with an Ecomet 3 base) beginning with wet 600 μm SiC paper (all polishing supplies were obtained from Buehler, Lake Bluff, IL). This was followed by polishing with 6 μm and then 3 μm aqueous diamond suspension (Metadi Diamond Suspensions) on Mastertex cloth. The final polish consisted of a 0.06 μm aqueous silica suspension (Mastermet Colloidal Silica Suspension) on Microcloth; this step also provided a slight chemical etch owing to the basic nature (pH 9.8) of the silica suspension. The samples were cleaned ultrasonically between each step and examined with an optical microscope to be certain that the scratches produced in the previous polishing step were adequately removed. Polishing cloths and papers were changed frequently to ensure efficient polishing without sample frictional heating. Typically, sample pressures of 7–18 kg

were necessary for high-purity Al in order to remove all of the scratches. Wheel speeds of up to 200 rpm were employed. After polishing was completed, most of the mounting epoxy was removed with a band saw and any remaining epoxy was dissolved by soaking in methylene chloride for several hours. To eliminate any film produced in the epoxy removal steps, samples were polished briefly by hand with the 0.06 μm silica suspension, copiously rinsed with deionized water, ultrasonically cleaned and blown dry with a stream of nitrogen.

For generation of films, a plastic clip was used to support the samples in the individual chromating baths. All chemicals used in the baths were reagent grade or better. After treatment, the samples were statically rinsed in deionized water and allowed to air dry. All samples were checked for the presence of a film using a scanning electron microscope (Amray 1820I) with an EDS (energy dispersive spectroscopy) attachment and Fourier transform infrared spectroscopy (Perkin Elmer, Model 1760X) used in the single reflection mode at 90° incidence before any surface science measurements were made.

Surface analyses were conducted at Evans East (Plainsboro, NJ). The AES measurements were made with a Perkin-Elmer Model 660 instrument using a 10 keV, 1.0 μA electron beam; areas of interest were selected using secondary electron imaging. For depth profiles, the 3 keV/3.4 μA argon ion beam (pressure = 25 mPa) was rastered over a 1 mm^2 area. Typically, three areas on the 2024 alloy samples were analyzed as a function of depth: the solid solution or matrix, a CuAl_2 θ -phase intermetallic and an $(\text{Fe}, \text{Mn})_3\text{SiAl}_{12}$ intermetallic. All sputter depths were obtained from sputter rates determined by calibration with an SiO_2 standard. For coated samples, a sputter rate of 350 \AA min^{-1} was used, while uncoated samples were sputtered at a rate of 30 \AA min^{-1} vs. SiO_2 . Quantitative AES results were determined from $dN(E)/d(E)$ spectra using standard PHI relative elemental sensitivity factors. The XPS measurements were made with a Perkin-Elmer Model 5000LS instrument. An Al anode x-ray source operating at 600 W and a take-off angle of 60° were used for all measurements, and analysis regions were typically $1 \times 3 \text{ mm}^2$. No depth profiling measurements were made with XPS. Chromium $2p_{3/2}$ curve fits were obtained using 85–100% Gaussian fits (with the remaining being Lorentzian). Linear background subtraction was employed.

All electrochemical measurements were performed with an EG&G Model 273 potentiostat. The cell was a Model K0235 flat cell made of glass and polypropylene. A Teflon O-ring seal was used to expose a 1 cm^2 area of the polished 1.90 cm diameter sample to the electrolyte. The counter electrode was a 6.45 cm^2 Pt screen and the reference electrode was Ag/AgCl (0.197 V vs. H_2/H^+), which was encased in a glass tube and separated from the electrolyte in contact with the electrodes by Vycor glass. A small Teflon tube acted as the Luggin capillary and was placed $\sim 1 \text{ mm}$ from the working electrode surface. The electrolyte was a pH 9.25 boric acid-sodium tetraborate mixture (0.11 g $\text{H}_3\text{BO}_3 + 22.00 \text{ g Na}_2\text{B}_4\text{O}_7 \cdot 10\text{H}_2\text{O}$ per liter of solution). At a pH of 9.25 both Al(III) and Cu(II) are nearly at the point of their lowest solubility,¹⁵ both of these species in the oxide or

Table 1. Atomic absorption analysis of aluminum alloy 2024-T3

Element	Wt. %	At. %
Iron	0.29	0.14
Manganese	0.62	0.31
Magnesium	1.40	1.60
Copper	4.40	1.90
Aluminum	93.29	96.02

hydroxide form should have been stable on the alloy surface.

RESULTS AND DISCUSSION

Metallurgy of aluminum-copper alloys

As most of the results reported in this paper were obtained using the aluminum-copper alloy 2024-T3 (hereafter referred to as 2024), a brief discussion of the metallurgy and its influence on the corrosion behavior of high Cu-containing Al alloys is warranted. Copper is one of the most important alloying elements for aluminum due to its appreciable solubility and the resulting strengthening effect.¹⁶ The Al-Cu phase diagram indicates that Cu has a maximum solubility in Al of 5.65 wt.% (2.53 at.%) at a temperature of 548 °C; the solubility decreases rapidly with temperature until very little solubility is observed at room temperature. This behavior is responsible for the phenomenon known as age hardening. In this process the Al-Cu mixture is heated above the solvus temperature in order to solubilize all of the Cu. The alloy is then rapidly quenched to room temperature, resulting in the formation of a supersaturated solution which is unstable. A process known as precipitation hardening begins, which involves the formation of clusters of Cu atoms (called Guinier-Preston (GP) zones) on preferred Al crystallographic planes (usually parallel to the Al(100) crystallographic plane). The disk-like GP zones are ~30–50 Å in diameter and ~1000 Å apart in the fully aged condition. This room-temperature strengthening of the alloy is known as natural aging. Artificial aging can also be induced, where the alloy is heated to 100–200 °C to transform the zones into transition forms of CuAl₂ in extremely fine dispersion; this can result in even greater strengthening. Heating above 250 °C causes the alloy to soften due to formation of bulk, incongruent (i.e. not parallel to any crystallographic plane), θ -phase CuAl₂. The notation used for natural and artificial aging is T3 and T6, respectively. This discussion of surface composition will focus only on the bulk-phase intermetallics, ~0.5–10 µm in size, in contact with the solid solution matrix. Imaging techniques were not available to monitor the much smaller GP and translational CuAl₂ zones.

Unfortunately, the composition of commercial Cu-Al alloys is more complex than that just outlined. These alloys contain several other alloying elements (either added or present as impurities, with Fe being the major impurity found in all Al alloys) which lead to the formation of a complex, multiphase structure. For example, 2024 contains appreciable amounts of Mg, Mn, Si and Fe which react during the alloying process to form bulk-phase intermetallics of composition Al₂CuMg, Al₇Cu₂Fe and (Mn, Fe)₃SiAl₁₂, in addition to CuAl₂. These intermetallic phases were easily identified through the use of SEM/EDS measurements conducted on highly polished 2024 surfaces. The CuAl₂ and (Mn, Fe)₃SiAl₁₂ intermetallic phases were found to predominate on 2024 and their appearance was very different. The CuAl₂ intermetallics were spherical and ~1 µm in diameter, while the Fe-containing phases were of irregu-

lar shape and ~10 µm along their longest direction. The AES analyses reported in this paper focus on three different regions: the CuAl₂ and (Mn, Fe)₃SiAl₁₂ intermetallic phases (denoted as Cu IM and Fe IM, respectively) and the solid solution matrix (denoted as matrix).

Given the large compositional difference between these intermetallic phases and the solid solution, one would expect these phases to be either anodic or cathodic to the solid solution.¹⁷ This would result in the formation of small galvanic couples across the surface which would enhance the formation of localized corrosion cells. Indeed, Cu greatly accelerates the corrosion rate of Al, presumably due to the formation of such galvanic couples. Micropitting has been observed to increase with additions of Cu to Al, especially as the size and density of CuAl₂ precipitates increase,¹⁷ and electrochemical pitting potentials obtained for Al-Cu alloys were found to be strongly influenced by the Cu content and aging conditions of the alloy.¹⁸ Scanning AES was used to probe the differences in oxidation rate across the 2024 surface exposed to electrochemical open-circuit conditions. In addition, the mechanism of corrosion protection afforded by Cr-containing conversion coating films was explored through scanning AES and XPS measurements.

Open-circuit behavior

The open-circuit behavior of high-purity Cu and Al and 2024 in a pH 9.25 boric-borate electrolyte is illustrated in Fig. 1. Also shown is the open-circuit behavior of 2024 in the same electrolyte containing different concentrations of CrO₃. A difference of nearly 1300 mV exists between the open-circuit potentials for pure Al and Cu, the two principal metals which make up the 2024 alloy; this large difference represents the relative ease of oxidation of Al over that of Cu. The 2024 surface displays an interesting behavior: an 'induction period' is observed where the open-circuit potential first decreases nearly 600 mV and then increases until it reaches a steady-state value of about -350 mV after ~2 h in the electrolyte. A straightforward explanation for this behavior is

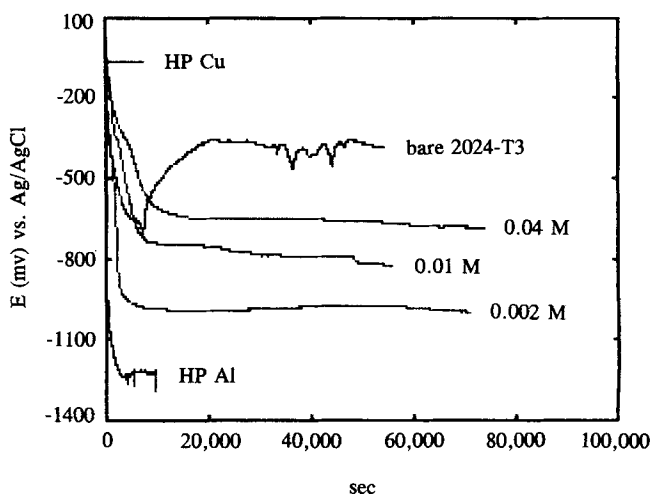


Figure 1. Open-circuit behavior of high-purity (HP) Cu, HP Al and aluminum alloy 2024-T3 in pH 9.25 boric-borate electrolyte, and 2024-T3 in electrolyte/indicated concentration of CrO₃.

that the surface initially shows Al-like behavior, as indicated by the drop in potential; the reaction associated with this Al-like behavior reaches steady state and a second process begins which imparts Cu-like behavior to the surface, indicated by the rise in potential. Addition of CrO_3 , however, negates this behavior; only the initial drop in open-circuit potential was observed.

The positive open-circuit potential (relative to high-purity Al) observed for 2024 in the boric-borate electrolyte with no CrO_3 added is not indicative of an increase in corrosion resistance of 2024 relative to high-purity Al. Likewise, the reduction of the open-circuit potential observed in the presence of CrO_3 does not represent a decrease in corrosion resistance. The open-circuit value simply represents the voltage obtained due to equilibrium between the anodic (oxidation) and cathodic (reduction) processes, which is quite complicated in Al alloys due to the number of metals present having different standard reduction potentials. The anodic reaction certainly involves the oxidation of several different metals in varying chemical states (i.e. solid solution matrix *vs.* intermetallic), while the cathodic processes are likely to be a mixture of both oxygen reduction and hydrogen evolution reactions.

In an attempt to explain the open-circuit behavior of 2024, scanning AES measurements combined with sputter depth profiling were conducted on the bare 2024 surface and 2024 exposed to open-circuit conditions for $\sim 60\,000$ s in the boric-borate electrolyte with and without the addition of 0.01 M CrO_3 . The surface elemental concentrations and the approximate film thicknesses are shown in Table 2 for three different areas on each surface: the solid solution matrix, a Cu intermetallic and an Fe intermetallic. The surface composition of the bare surface is not that expected from the bulk composition (see Table 1). The Cu is highly enriched on the matrix (17 at.% *vs.* a bulk value of 1.9 at.%) while being depleted at the Cu intermetallic (one would expect 55 at.% Cu if it were pure CuAl_2). Copper is also found on the Fe intermetallic, suggesting that it is soluble in this intermetallic. Depth profiles of these thin films are shown in Figs 2–4, where $N(E)$ data are shown for individual elements as a function of number

of sputter cycles. Copper is easily seen to be highly enriched on both the matrix and the Fe intermetallic (Figs 2 and 4), while Fe is depleted at the surface of the Fe intermetallic. These Cu-enriched layers appear to be nearly twice as deep as the oxide layer thickness and once the ~ 50 Å oxide layer (in agreement with previous XPS thickness measurements)¹⁹ is removed by sputtering, the Cu peaks at a concentration nearly twice that found on the matrix. The source of this enriched Cu layer on the surface is not known; possibilities include diffusion from the bulk, oxidative removal of the Al from the solid solution or re-deposition of oxidized Cu from the intermetallic regions onto the matrix during polishing. Re-deposition has been hypothesized to occur during dissociation of θ -phase CuAl_2 .²⁰ The increase of Cu concentration with sputter depth on the CuAl_2 intermetallic (Fig. 3) appears to track the oxide thickness; once the oxide is removed, the Cu reaches the fixed bulk concentration expected for the Cu intermetallic. Interestingly, Mg is enriched on the Cu intermetallic.

Comparison of the bare 2024 surface AES data with that for the surface exposed to the boric-borate electrolyte indicates that the enriched Cu layer found on the matrix has nearly been removed and the Cu remains highly enriched on the Fe intermetallic (note regarding Table 2: both intermetallics are Fe intermetallics in this case). Depth profiles indicate that significant oxide film growth has occurred on both the matrix and Fe intermetallics, with the matrix yielding the thickest film. These differences in film thickness suggest that the intermetallics are cathodic to the matrix, which results in a galvanic couple that accelerates oxidation of the matrix. The profile for the matrix (Fig. 5) indicates that the film is practically all aluminum oxide which has grown over the enriched Cu layer found on the bare surface; the enriched Cu layer is now observed at the film/surface interface. An enriched Cu layer is observed on the Fe intermetallic, and from the depth profile (not shown), the Cu appears to be in the oxidized state, for the oxygen tracks the Cu behavior. Therefore, exposure to open-circuit conditions appears to form a surface with a relatively thick aluminum oxide (probably an

Table 2. Surface composition of films on aluminum alloy 2024-T3 at open-circuit potential^a as determined by AES

Sample	Al	O	Atomic per cent		Cr	C	Approximate film thickness (Å)
			Cu	Fe			
Untreated							
Matrix	50.9	19.8	17.2	—	n/a ^b	10.0	50
Cu IM	28.3	28.8	18.0	—	n/a	8.7	50
Fe IM	31.8	18.5	35.8	4.7	n/a	3.8	50
In buffer							
Matrix	61.3	33.7	1.7	—	n/a	2.0	1500
Cu IM ^c	29.1	15.3	36.2	—	n/a	14.0	1000
Fe IM	24.5	18.6	43.1	2.6	n/a	6.1	600
In CrO_3							
Matrix	31.7	38.5	12.9	—	3.9	12.3	450
Cu IM	34.1	27.4	23.5	—	1.7	11.0	150
Fe IM	16.3	21.7	16.2	2.4	4.4	31.0	150

^a Samples were exposed to open-circuit conditions for $\sim 60\,000$ s.

^b n/a: not applicable.

^c Not true CuAl_2 intermetallic; Fe found later in profile.

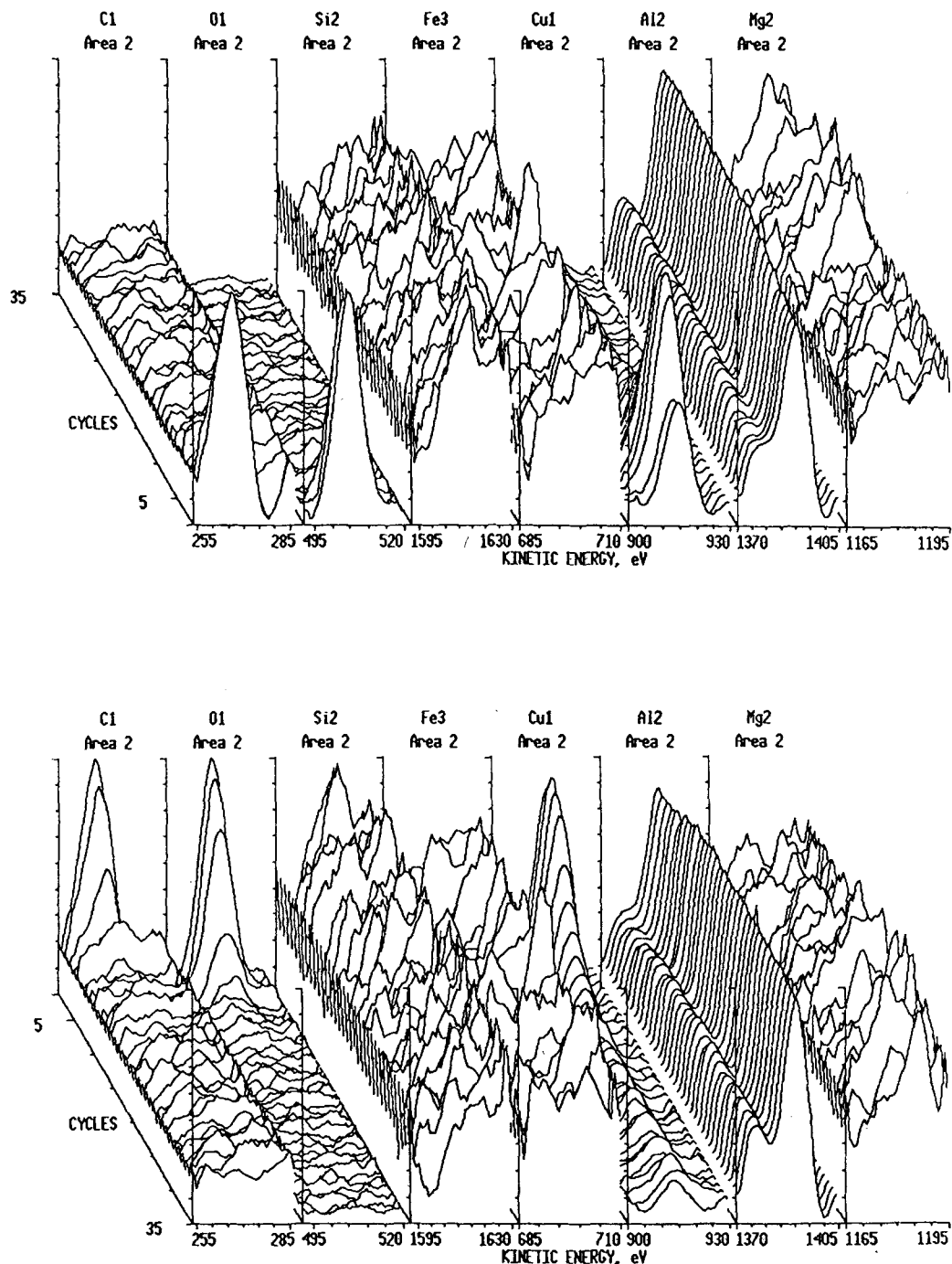


Figure 2. Auger electron spectroscopy depth profile of aluminum alloy 2024-T3 solid solution matrix subjected to mechanical polishing only. Total depth of profile ~ 300 Å and ~ 8.6 Å per cycle. Front and back views.

hydroxide) layer in contact with Fe intermetallic areas containing enriched Cu, most likely in the form of hydroxide. These data fit very well with the mechanism proposed above. The initial Al-like behavior results from the oxidation of the matrix due to the galvanic couple caused by the presence of the intermetallics. This oxidation is rapid and quickly reaches steady state, probably due to limited ionic mobility caused by the thick overlayer, at which time the Cu-enrichment reaction, possibly driven by both Al and Cu oxidation, begins on the intermetallics. The closer to Cu-like rather than Al-like behavior observed with the open-circuit potential after the initial induction period must

be attributed to enrichment of the Cu on the intermetallic phases.

Addition of 0.01 M CrO_3 to the boric-borate electrolyte clearly inhibits film formation on both the matrix and intermetallics, as indicated by the approximate film thicknesses listed in Table 2. Although the concentration is low, Cr is found incorporated throughout the film (depth profile not shown). A reduction in Al concentration is observed on the matrix compared to the polished sample and the surface exposed to electrolyte without added CrO_3 . Copper is now enhanced on the surface of the matrix, which is opposite to that observed without CrO_3 present. Iron is depleted at the surface of

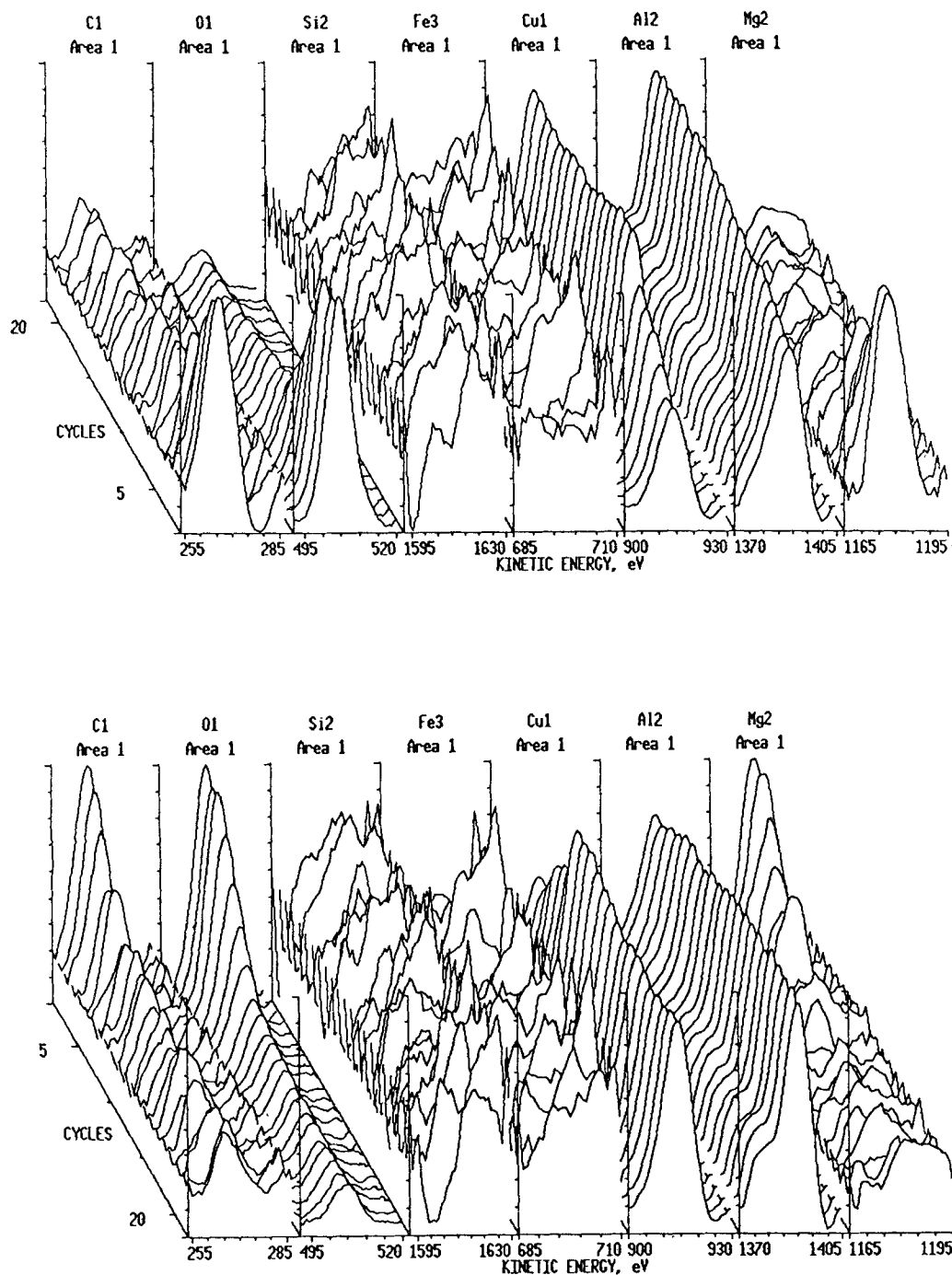


Figure 3. Auger electron spectroscopy depth profile of aluminum alloy 2024-T3 Cu intermetallic subjected to mechanical polishing only. Total depth of profile ~ 180 Å and ~ 7.8 Å per cycle. Front and back views.

the Fe intermetallic, as is the case with the polished surface and the surface exposed to electrolyte only. Therefore, the presence of CrO_3 , in addition to forming a Cr-containing layer, appears to produce a surface which contains a more uniform concentration of both Al and Cu. This may be partly responsible for the observed decrease in oxidation rate.

Open-circuit potentials were also recorded for 2024 immersed in the boric-borate electrolyte containing 3 mM $\text{K}_4\text{Fe}(\text{CN})_6$ and 3 mM $\text{K}_3\text{Fe}(\text{CN})_6$ (ferro- and ferricyanide, respectively) since these species are believed to improve the corrosion resistance obtained from commercial chromating solutions. Figure 6 compares the

open-circuit behavior with that obtained with neither cyanide present. Addition of ferricyanide lessens the duration of the initial induction period compared to the bare surface and the steady-state open-circuit potential is ~ 150 mV more positive than for the bare alloy. The sample immersed in the ferrocyanide-containing solution, however, has the opposite effect; the induction period is longer and the stable open-circuit potential is nearly 200 mV negative to that observed for the bare alloy. Although no AES measurements were made with these samples, the difference observed is believed to be due to the ability of ferrocyanide to react with the surface Cu (mostly on the intermetallics) to form an

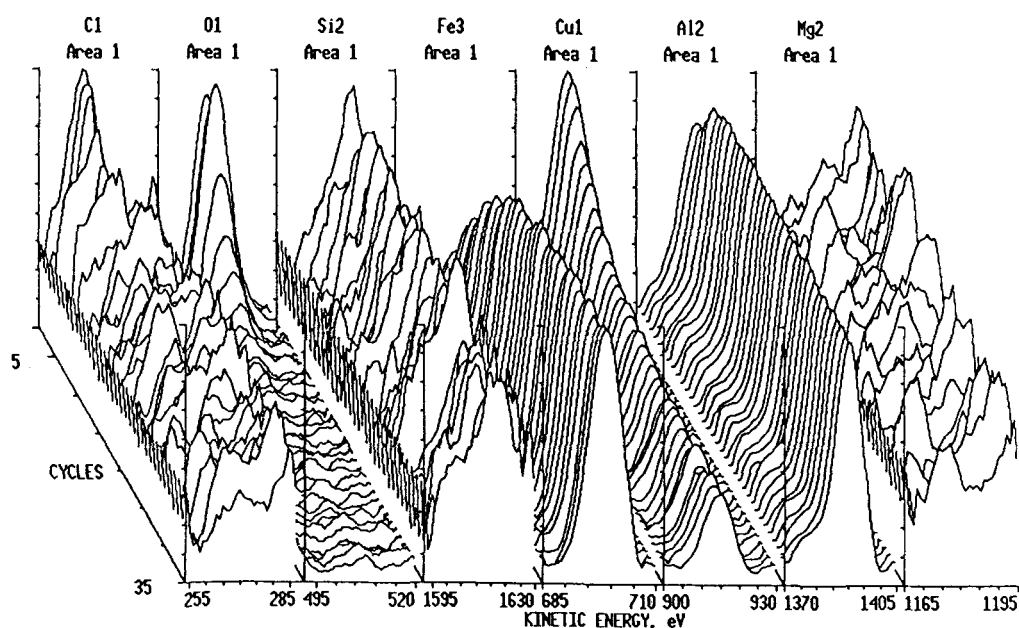


Figure 4. Auger electron spectroscopy depth profile of aluminum alloy 2024-T3 Fe intermetallic subjected to mechanical polishing only. Total depth of profile ~ 300 Å and ~ 8.6 Å per cycle. Back view.

insoluble copper ferrocyanide. This reduces the galvanic behavior addressed above. This behavior will be discussed in more detail in the following sections.

Chemically formed Cr-based coatings

Commercial chromating of Al alloys involves the formation of Cr-containing films from acidic solutions (pH 1) of $\text{CrO}_3 + \text{NaF}$. The most corrosion-resistant formulations also contain either potassium ferro- or ferricyanide. The following AES and XPS data were obtained from films generated with these species. Unless noted, the concentrations used in all of these studies were 40 mM CrO_3 , 12 mM NaF and 3 mM ferro- or ferricyanide.

$\text{CrO}_3 + \text{NaF}$. In Table 3 are shown the AES-determined elemental surface concentrations of films generated on 2024 by immersion in $\text{CrO}_3 + \text{NaF}$ for three different immersion times. For all the films, the concentration of Cr and O found on the solid solution matrix is nearly the same. Fluorine is found on the surface of some of the films but depth profiles do not indicate its presence below the surface; its absence could be due to removal by vacuum sublimation of HF, which could form owing to the presence of water in the film. Very little or no Al is found on the matrix surfaces, which is considered advantageous from a corrosion inhibition standpoint. The surfaces of the intermetallics, on the other hand, are only slowly covered by the growing film; after 1.5 and 3 min, appreciable amounts of Cu and Al are still present on the intermetallic surfaces. However, after 5 min the surfaces of the intermetallic regions are almost totally composed of Cr and O, with an overall composition very similar to that found on the surface of the matrix. The homogeneous surface composition of this film after 5 min is likely to be responsible for the high corrosion resistance of these coatings. In addition, the mode of growth observed here, i.e. rapid growth on the solid

solution matrix with slower growth on the intermetallics, is in good agreement with the mechanism of oxidation observed under the open-circuit conditions discussed above.

A depth profile taken from the solid solution matrix for the film obtained with a 3 min immersion in $\text{CrO}_3 + \text{NaF}$ is shown in Fig. 7. Oxygen and Cr track each other very closely through the entire depth of the film. Aluminum, although not present on the surface, is found in the Cr + O layer, indicating that it is an integral part of the film. Also, the enriched Cu layer found at the surface of the polished sample remains intact during film formation; this Cu, like the intermetallics, probably assists in accelerating the oxidation of Al in the matrix. Depth profiles taken from the intermetallic regions show similar behavior as observed earlier: depletion of Fe and an enhancement of Cu on the surface of the Fe intermetallic (for immersion times of

Table 3. Surface composition of films obtained by immersion of aluminum alloy 2024-T3 in 40 mM $\text{CrO}_3 + 12$ mM NaF at the indicated times as determined by AES

Sample	Atomic per cent						
	Al	O	Cu	Cr	Fe	C	F*
1.5 min							
Matrix	—	57.9	—	39.3	—	0.6	N
Cu IM	12.1	36.5	15.5	23.6	1.4	4.2	N
Fe IM	34.7	20.0	11.8	18.5	3.7	8.6	N
3.0 min							
Matrix	—	60.5	—	36.9	—	—	Y
Cu IM	19.7	36.9	12.5	25.6	—	2.7	Y
Fe IM	25.6	33.0	11.4	22.3	2.5	2.9	Y
5.0 min							
Matrix	3.4	58.5	—	34.7	—	1.7	Y
Cu IM	3.4	51.1	2.7	37.9	—	2.2	Y
Fe IM	2.7	58.3	—	35.2	—	2.3	Y

* Fluorine concentrations were uncertain owing to probable release of HF from coatings under vacuum, conditions. N = No; Y = Yes.

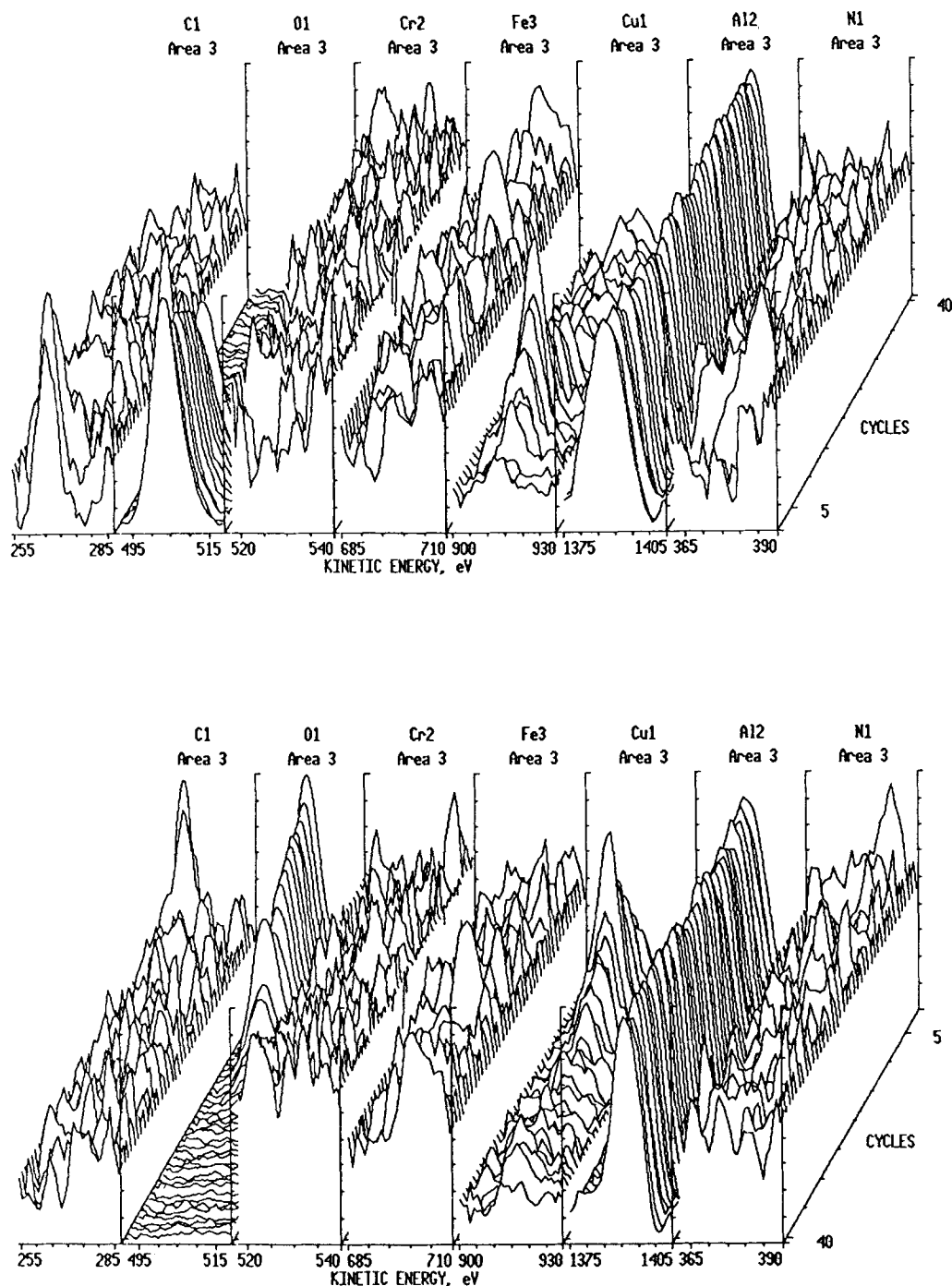


Figure 5. Auger electron spectroscopy depth profile of aluminum alloy 2024-T3 solid solution matrix exposed to pH 9.25 boric-borate electrolyte at open-circuit potential for $\sim 60\,000$ s. Total depth of profile ~ 4200 Å and ~ 102 Å per cycle. Front and back views.

≤ 3 min) and depletion of Cu on the surface of the Cu intermetallic. The thickness of various films as estimated from the depth profiles is illustrated in Table 4. Very good agreement was observed between the depth profile-determined thicknesses on the matrix and those measured with a Dektak 3030ST surface profiler, which was scanned over portions of the samples masked off with tape. Some of these films were obtained by treatment in $\text{K}_4\text{Fe}(\text{CN})_6^-$ and $\text{K}_3\text{Fe}(\text{CN})_6^-$ -containing solutions, which are discussed in detail below. As observed with nearly all the samples coated for 1.5 and 3 min, the film deposition rate (and, thus, the oxidation rate) proceeds in the following order: matrix $>$ Cu IM $>$ Fe IM.

After a 5 min immersion, however, the film thickness on the matrix and the intermetallics is approximately the same. This can be attributed to the slow oxidation rate of the intermetallic phases with respect to the matrix; the film on the matrix rapidly reaches its steady-state thickness while the intermetallic films require longer times. Eventually, however, like the concentration gradient across the surface, the thickness gradient is minimized and a more corrosion-resistant surface is presumably formed.

$\text{CrO}_3 + \text{NaF} + \text{K}_4\text{Fe}(\text{CN})_6$ or $\text{K}_3\text{Fe}(\text{CN})_6$. In Table 5 are shown the surface compositions of films generated from

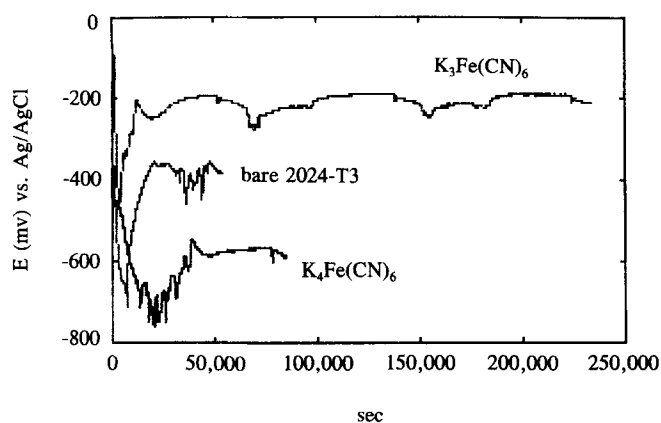


Figure 6. Open-circuit behavior of aluminum alloy 2024-T3 in pH 9.25 boric-borate electrolyte with and without the addition of 3 mM $K_4Fe(CN)_6$ and $K_3Fe(CN)_6$.

baths containing $CrO_3 + NaF + K_4Fe(CN)_6$ (ferro) or $K_3Fe(CN)_6$ (ferri). For ease of comparison, data from Table 4 for films generated without ferro- or ferricyanide are included in Table 5. The presence of either ferro- or ferricyanide on the surface was monitored by the N concentration and, to some extent, Fe concentration; although its trend was similar to that found for N, C was not chosen as the tracking element owing to the complication arising from possible contamination. Nitrogen can be observed over the entire surface of each film. Larger concentrations, however, are localized in all films on the intermetallic phases, suggesting that both ferro- and ferricyanide are preferentially deposited onto these regions. This is further substantiated by comparing the depth profiles shown in Figs. 8 and 9. The ferricyanide is not found through the entire matrix film thickness; instead, as indicated by both C and N, it extends ~ 200 Å into the film compared to a total film thickness of ~ 1000 Å. For the Cu intermetallic, the ferricyanide is found to extend through the entire film

Table 4. Approximate thickness for indicated films on aluminum alloy 2024-T3 as determined by AES depth profiles

Sample ^a	Area	Thickness (Å)
$CrO_3 + NaF$, 1.5 min	Matrix	750–875
	Fe IM	88–140
	Cu IM	610–750
$CrO_3 + NaF + ferri$, 1.5 min	Matrix	823–910
	Fe IM	105–175
	Cu IM	263–315
$CrO_3 + NaF + ferro$, 1.5 min	Matrix	770–840
	Fe IM	175–280
	Cu IM	350–438
$CrO_3 + NaF$, 3.0 min	Matrix	1050–1225
	Fe IM	263–420
	Cu IM	438–612
$CrO_3 + NaF + ferri$, 3.0 min	Matrix	980–1120
	Fe IM	438–525
	Cu IM	385–438
$CrO_3 + NaF + ferro$, 3.0 min	Matrix	1015–1085
	Fe IM	315–455
	Cu IM	840–1015
$CrO_3 + NaF$, 5.0 min	Matrix	1350–1500
	Fe IM	1200–1350
	Cu IM	1200–1350

^a 'ferri' denotes $K_3Fe(CN)_6$; 'ferro' denotes $K_4Fe(CN)_6$.

thickness (Fig. 9), as evidenced by comparing the C and N profiles with that of Cr and O. The same behavior is found on the Fe intermetallic. Fourier transform infrared spectra obtained from all surface films generated from solutions containing either ferro- or ferricyanide displayed bands at ~ 2080 cm^{-1} , verifying that the C and N was present as CN.

Previous wet chemical analyses¹ indicated that ferricyanide-accelerated film growth proceeded through

Table 5. Surface composition of films obtained by immersion of aluminum alloy 2024-T3 in indicated solutions as determined by AES

Sample ^a	Area	Atomic per cent						
		Al	O	Cr	F	Fe	Cu	N
$CrO_3 + NaF$, 1.5 min	Matrix	—	57.9	39.3	—	—	—	—
	Fe IM	34.7	20.0	18.5	—	3.7	11.8	—
	Cu IM	12.1	36.5	23.6	—	1.4	15.5	—
$CrO_3 + NaF + ferri$, 1.5 min	Matrix	—	44.8	26.1	2.3	1.6	1.1	11.1
	Fe IM	—	24.2	17.8	1.4	5.8	3.1	20.9
	Cu IM	—	18.4	13.2	1.2	3.4	12.1	11.2
$CrO_3 + NaF + ferro$, 1.5 min	Matrix	—	48.0	29.7	—	1.8	1.3	9.0
	Fe IM	11.7	21.8	15.9	—	2.8	9.0	17.4
	Cu IM	3.9	18.0	10.8	—	2.5	14.5	19.3
$CrO_3 + NaF$, 3.0 min	matrix	—	60.5	36.9	1.0	—	—	—
	Fe IM	25.6	33.0	22.3	1.0	2.5	11.4	—
	Cu IM	19.7	36.9	25.6	1.3	—	12.5	—
$CrO_3 + NaF + ferri$, 3.0 min	Matrix	—	46.4	30.6	1.9	1.9	1.1	7.9
	Fe IM	—	23.5	16.6	—	6.5	—	19.4
	Cu IM	—	16.9	14.6	0.9	1.1	16.9	19.9
$CrO_3 + NaF + ferro$, 3.0 min	Matrix	4.6	41.6	26.2	1.9	2.1	1.4	10.0
	Fe IM	6.3	17.3	12.5	—	3.7	9.2	21.8
	Cu IM	8.2	26.1	18.8	—	3.2	6.2	15.1

^a 'ferri' denotes $K_3Fe(CN)_6$; 'ferro' denotes $K_4Fe(CN)_6$.

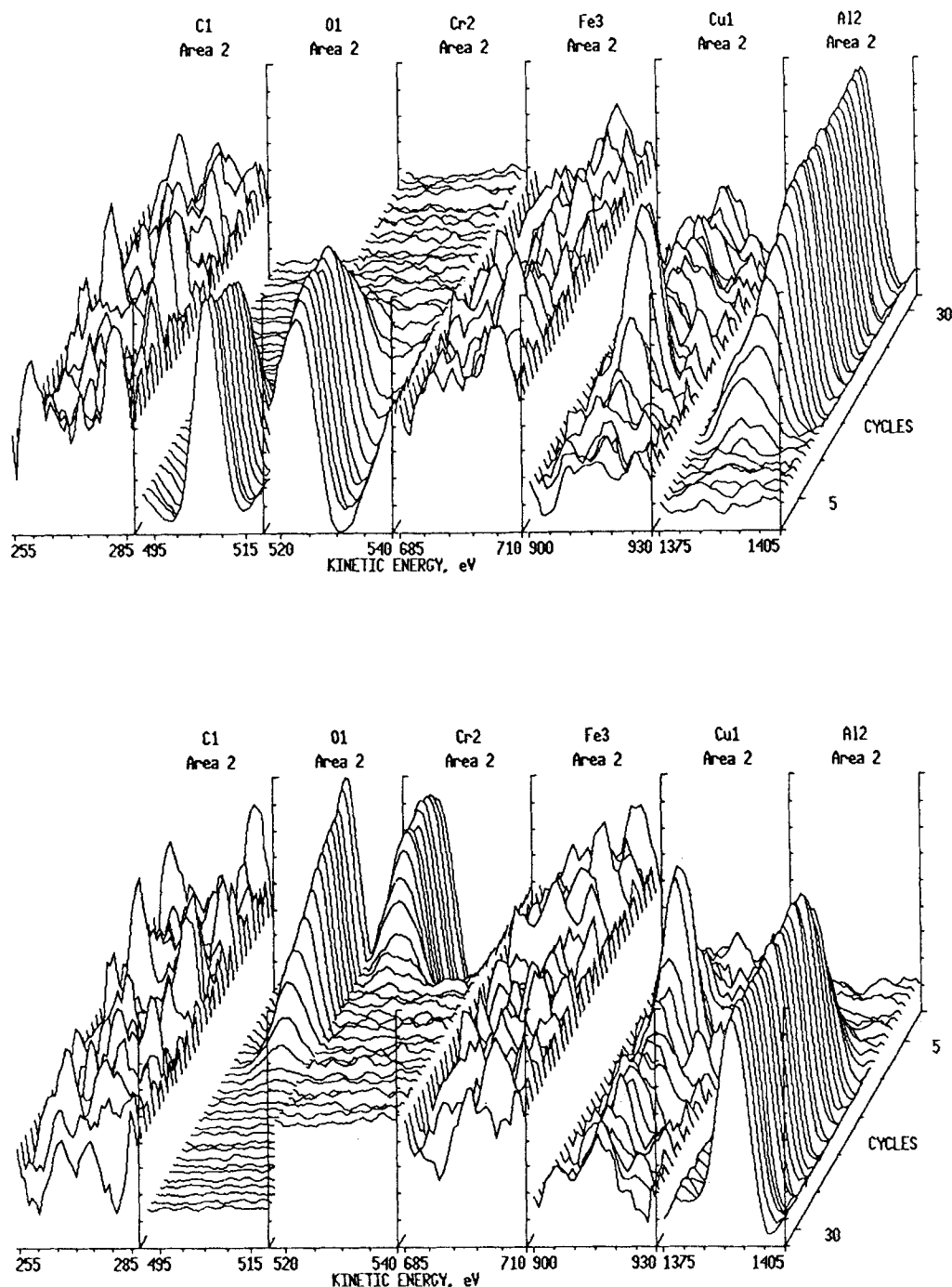


Figure 7. Auger electron spectroscopy depth profile of aluminum alloy 2024-T3 solid solution matrix exposed to 40 mM CrO_3 + 12 mM NaF for 3 min. Total depth of profile ~ 3150 Å and ~ 95 Å per cycle. Front and back views.

incorporation of $\text{CrFe}(\text{CN})_6$ into the film. The type of Al used in these studies was not mentioned. The XPS measurements obtained from films generated on 99.8% Al showed that the ferricyanide was concentrated on the surface,^{3,4} as found here on the solid solution matrix, and a mechanism was suggested whereby accelerated film growth resulted from adsorption of ferricyanides on the surface of the precipitating Cr-O particles.⁴ The substrate in these studies was chosen in order 'to minimize uncertainties due to the presence of alloying elements', even though only alloyed Al is commercially treated, generally. Our results on Al-Cu alloy 2024 indicated that the cyanide-containing species was concen-

trated on the intermetallic regions and we believe that this is due to reaction of the ferri- or ferrocyanide with Cu. Both Cu(I) and Cu(II) are known to react with ferrocyanide²¹ to form $\text{Cu}_4\text{Fe}(\text{CN})_6$ and $\text{Cu}_2\text{Fe}(\text{CN})_6$, respectively, both of which are known to be insoluble in water. An aluminum ferrocyanide will form, but only with considerable difficulty.²¹ Simple mixing experiments indicated that Cu(I) and Cu(II) do react with the ferrocyanide ion to form insoluble precipitates while the ferricyanide ion produces a color change but not a precipitate. This difference in solubilities between copper ferro- and ferricyanides is likely to be responsible for the open-circuit behavior observed in Fig. 6. In addi-

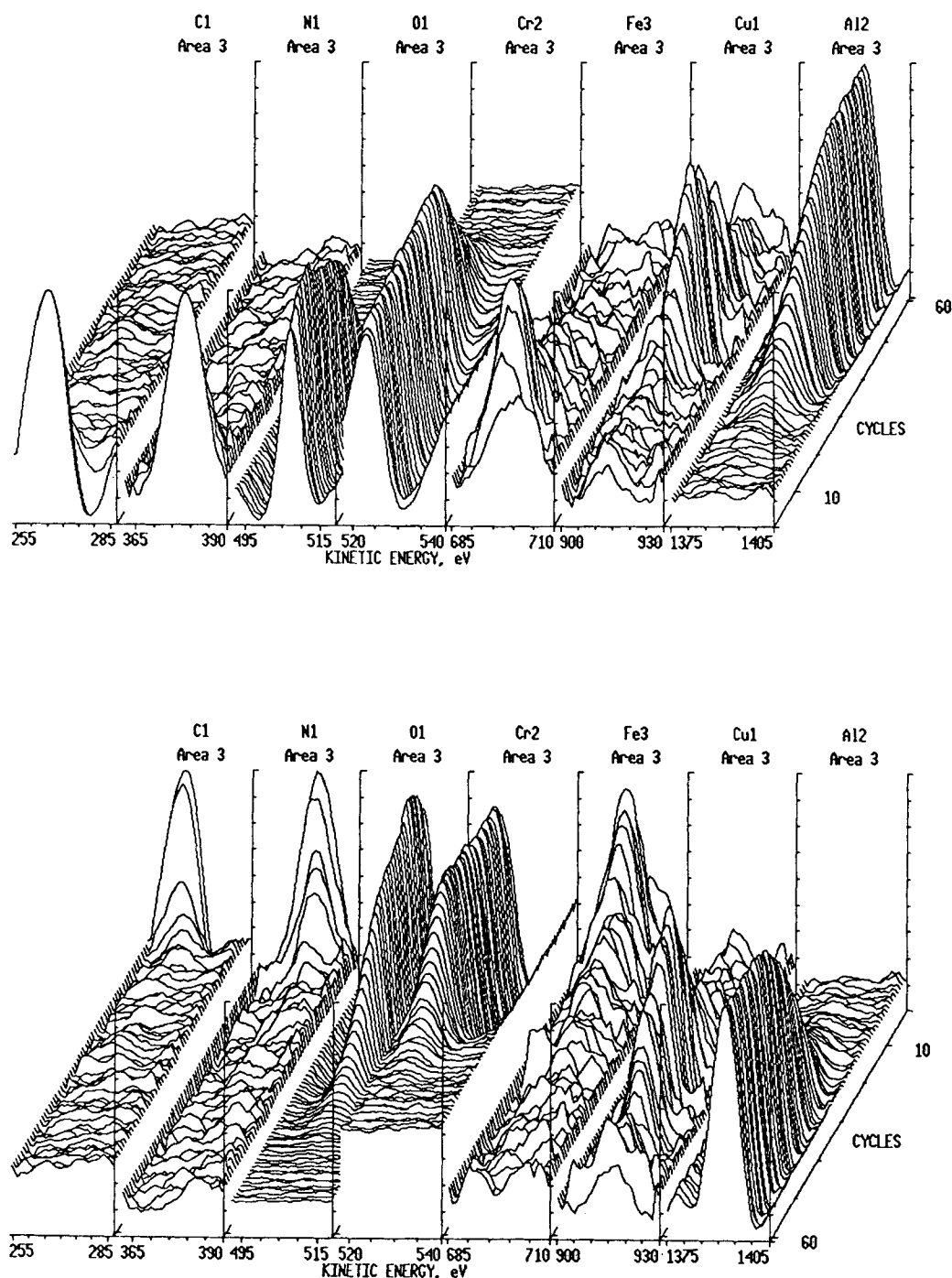


Figure 8. Auger electron spectroscopy depth profile of aluminum alloy 2024-T3 solid solution matrix exposed to 40 mm CrO_3 + 12 mm NaF + 3 mm $\text{K}_3\text{Fe}(\text{CN})_6$ for 3 min. Total depth of profile ~ 2100 Å and ~ 35 Å per cycle. Front and back views.

tion, XPS measurements indicate that the Fe on the surface was Fe(II) (as in ferrocyanide), suggesting that ferrocyanide is responsible for the enhanced C and N found throughout the films on the intermetallic phases. This data must be taken with some caution, however, for Fe(III) found in these films is known to undergo x-ray beam-induced reduction.⁴ The beneficial properties derived from having either ferro- or ferricyanide present in the chromating bath are, thus, believed to be due to reaction of these species with the Cu in the intermetallic phases. The advantage of this reaction is to

reduce the magnitude of the galvanic couple that exists between the matrix and the intermetallic phases.

X-ray photoelectron spectroscopy measurements

XPS measurements were undertaken with a number of films generated from both ferro- and ferricyanide-containing solutions on high-purity Al and 2024 in order to determine the chemical state of Cr. Wet chemical methods,²² XPS measurements¹³ and XANES

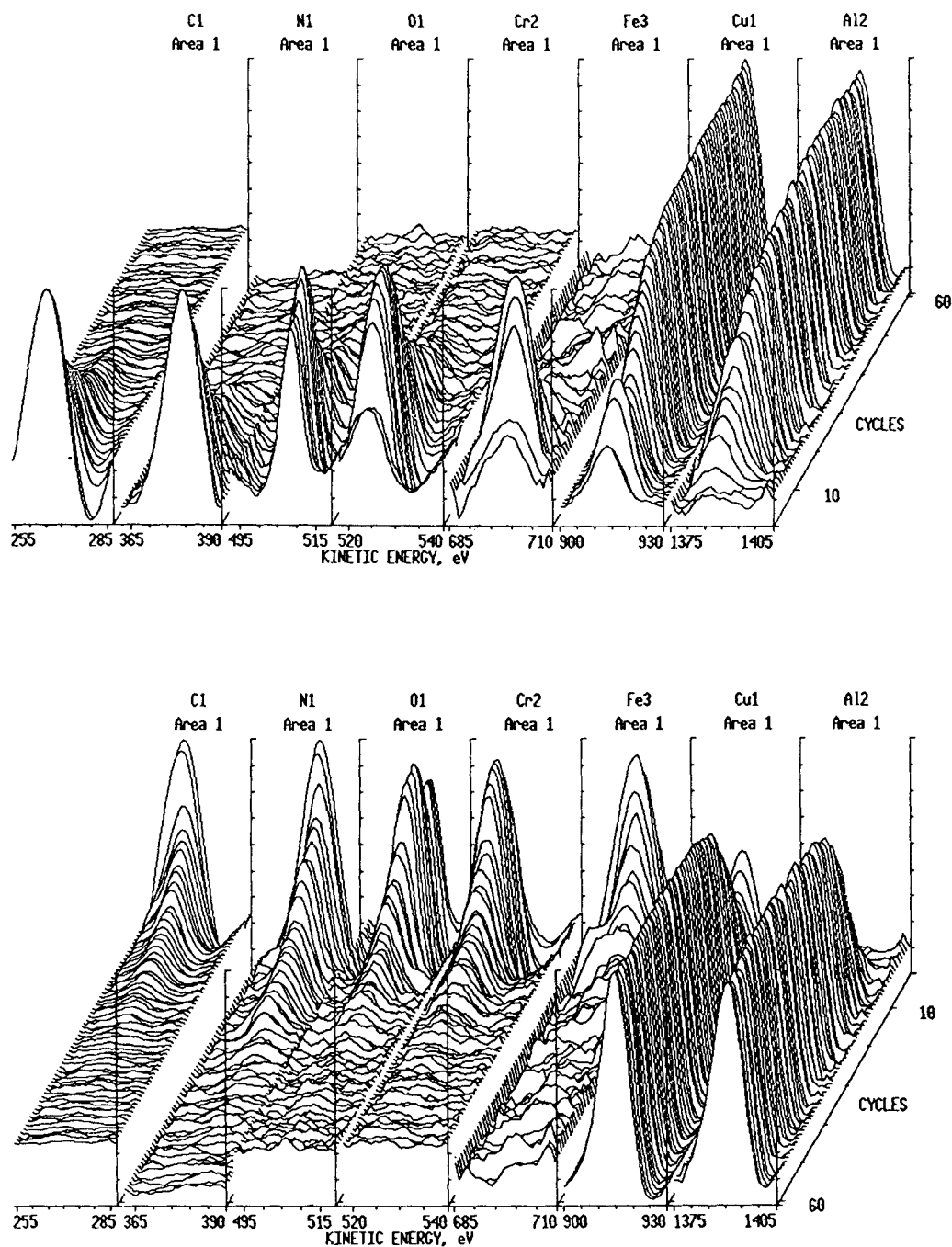


Figure 9. Auger electron spectroscopy depth profile of aluminum alloy 2024-T3 Cu intermetallic exposed to 40 mm CrO_3 + 12 mm NaF + 3 mm $\text{K}_3\text{Fe}(\text{CN})_6$ for 3 min. Total depth of profile ~ 2100 Å and ~ 35 Å per cycle. Front and back views.

measurements¹⁴ have shown that similar Cr-containing films contain significant concentrations of Cr(VI) in addition to the expected Cr(III). The presence of Cr(VI) in the film is believed to impart a 'self-healing' nature to the film because Cr(VI) would be available to form an insoluble Cr(III) species upon oxidative attack of the surface, as occurs during corrosion. A typical fitted XPS spectrum is shown in Fig. 10 and the binding energies of the individual peaks along with the percentage of the total Cr concentration are shown in Table 6. The low- and high-binding energy Cr $2p_{3/2}$ peaks indicate the presence of Cr(III) and Cr(VI) species, respectively, with the likely candidates being Cr_2O_3 (binding energy = 576.3 eV) and CrO_4^{2-} (binding energy = 579.3

eV).^{23,24} Assignment of the middle peak is uncertain since it lies between that for CrOOH (binding energy = 577.0 eV) and CrO_3 (binding energy = 578.3 eV); the formation of this peak, however, may be due to x-ray-induced reduction of the Cr(VI) species,^{23,25} although no studies were performed for verification. If one compares the percentage of the Cr(III) peak with that of the sum of the percentages of the Cr(VI) peak and the middle peak for all of the treatments shown in Table 6, a ratio of $\sim 60:40$ Cr(VI):Cr(III) is obtained in most cases, assuming that the middle peak was also due to the presence of a Cr(VI) species. Chemical analysis of similar films has shown that $\sim 60\%$ of the Cr is in the form of Cr(VI)²² while XANES¹⁴ and XPS¹³ indicate

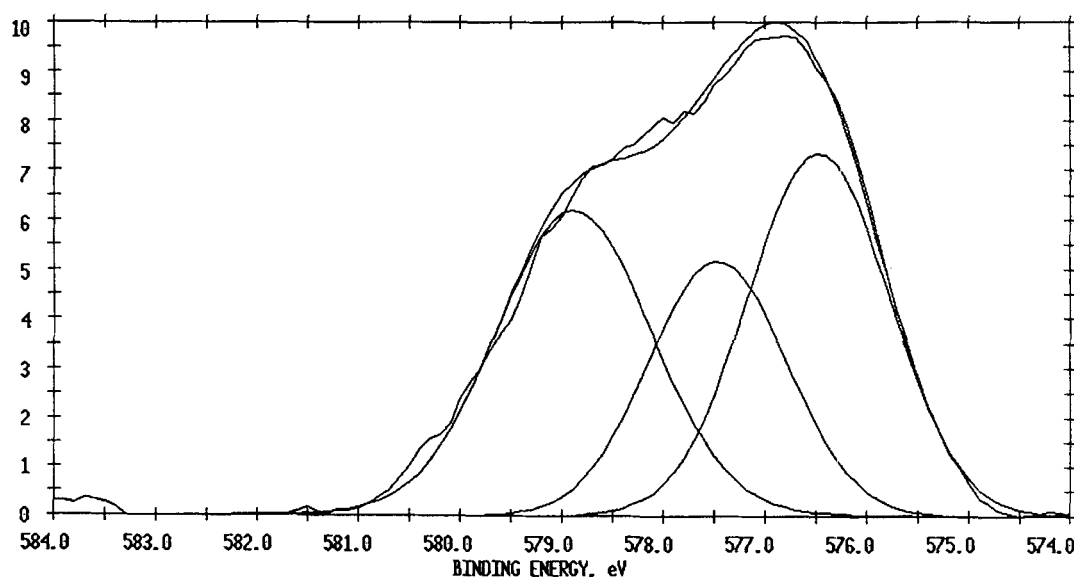


Figure 10. Cr $2p_{3/2}$ XPS spectrum of high-purity Al exposed to 40 mM CrO_3 + 12 mM NaF + 3 mM $\text{K}_3\text{Fe}(\text{CN})_6$ for 3 min. (100% Gaussian fit.)

that $\sim 20\%$ and $\sim 9\%$, respectively, of the Cr is Cr(VI). Both of these analyses were bulk film analyses, while the present data are surface concentrations. All of these analyses could be dependent on the substrate (type of high-purity or alloy, alloy aging conditions, composition of intermetallics, etc.), the surface pretreatment

conditions (polishing *vs.* chemical cleaning and de-oxidation) and coating conditions of the chromating bath (composition, time, temperature, etc.). What is evident is that a significant concentration of Cr is available to promote film 'self-healing'.

Table 6. Surface concentration and chemical state of Cr for indicated films on high-purity Al and aluminum alloy 2024-T3 as determined by XPS^a

Sample ^b	Cr $2p_{3/2}$ binding energy (eV)	Percentage of total Cr area
2024 in ferri, 1.5 min	576.7 ^c	57.85
	578.1	28.80
	579.2 ^d	13.36
2024 in ferri, 3.0 min	576.4	38.50
	577.4	31.94
	578.8	29.57
2024 in ferro, 1.5 min	576.5	39.90
	577.6	36.30
	579.0	23.81
2024 in ferro, 3.0 min	576.4	41.62
	577.6	32.41
	579.0	25.96
HP Al in ferri, 1.5 min	576.6	39.67
	577.5	23.99
	578.8	36.34
HP Al in ferri, 3.0 min	576.5	37.87
	577.5	26.12
	578.9	36.00
HP Al in ferro, 1.5 min	576.5	38.51
	577.5	25.39
	578.8	36.10
HP Al in ferro, 3.0 min	576.4	31.09
	577.4	33.47
	578.9	35.44

^a All solutions contained 40 mM CrO_3 + 12 mM NaF + 3 mM ferro- or ferricyanide.

^b 'ferri' denotes $\text{K}_3\text{Fe}(\text{CN})_6$; 'ferro' denotes $\text{K}_4\text{Fe}(\text{CN})_6$.

^c Cr(III).

^d Cr(VI).

CONCLUSIONS

- (1) Under open-circuit and chromating bath conditions, the aluminum alloy 2024-T3 surface appears to oxidize in two discrete steps: the matrix rapidly oxidizes followed by slower oxidation of the CuAl_2 and $(\text{Mn}, \text{Fe})_3\text{SiAl}_{12}$ intermetallics.
- (2) Copper and its enrichment at the surface greatly influences the reactivity of aluminum alloy 2024-T3.
- (3) Intermetallic phases play an important role in determining the redox properties of aluminum alloy surfaces.
- (4) The enhanced corrosion resistance obtained by addition of ferricyanide to chromating baths is believed to be due to the formation of copper ferrocyanides on the metallic phases which alters their activity with respect to the solid solution matrix.
- (5) At adequate treatment times, the corrosion resistance of Cr films on aluminum 2024-T3 alloy is likely to be enhanced by the uniform surface composition of Cr and O, the absence of Al and Cu in the near-surface region and the uniform film thickness across both the solid solution matrix and the intermetallics.
- (6) A large concentration of Cr(VI) is available for film 'self-healing' during oxidative attack in all Cr films presented in this work. Approximately 60% of the surface Cr is believed to be Cr(VI), with the remaining being Cr(III).

Acknowledgements

The authors would like to thank Richard L. Moore and David. A. Cole of Evans East, Plainsboro, NJ for performing the AES and XPS measurements and Diane P. Halterman of Henkel Corporation for conducting the atomic absorption analysis.

REFERENCES

1. N. J. Newhard, Jr., *Met. Finish.* **70**, 49, 66 (1972).
2. W. Stumm, G. Furrer, E. Wieland and B. Zinder, *NATO ASI Series, Series C*, **149**, 55 (1985).
3. J. A. Treverton and N. C. Davies, *Met. Technol. N.Y.* **Oct.**, 480 (1977).
4. J. A. Treverton and N. C. Davies, *Surf. Interface Anal.* **3**, 194 (1981).
5. F. Altmayer, *Plating Surf. Finish.* **1**, 44 (1984).
6. D. M. Berger, *Met. Finish.* **11**, 25 (1983).
7. R. C. Furneaux, G. E. Thompson and G. C. Wood, *Corros. Sci.* **19**, 63 (1979).
8. J. A. Treverton and M. P. Amor, *J. Microsc.* **140**, 383 (1985).
9. G. M. Brown, K. Shimizu, K. Kobayashi, G. E. Thompson and G. C. Wood, *Corros. Sci.* **33**, 1371 (1992).
10. A. Quentmeier, H. Bubert, R. P. H. Garten, H. J. Heinen, H. Puderbach and S. Storp, *Mikrochim. Acta Suppl.* **11**, 89 (1985).
11. M. F. A. Rabbo, J. A. Richardson and G. C. Wood, *Corros. Sci.* **18**, 117 (1978).
12. R. J. Sunderland, *Jpn. J. Appl. Phys. Suppl.* **2**, 347 (1974).
13. K. Asami, M. Oki, G. E. Thompson, G. C. Wood and V. Ashworth, *Electrochim. Acta* **32**, 337 (1987).
14. M. W. Kendig, A. J. Davenport and H. S. Isaacs, *Corros. Sci.* **34**, 41 (1993).
15. J. Kragton, *Atlas of Metal-Ligand Equilibria in Aqueous Solution*. Halstead Press, NY (1978).
16. J. E. Hatch (ed.), *Aluminum: Properties and Physical Metallurgy*, Chapt. 5, pp. 143 ff. American Society for Metals, Metals Park, OH (1988).
17. J. R. Scully and D. E. Peebles, *National Electrochemical Society Meeting*, Spring, 1991, Extended Abstracts. The Electrochemical Society, Pennington, NJ (1991).
18. I. L. Muller and J. R. Galvele, *Corros. Sci.* **17**, 179 (1977).
19. B. R. Strohmeier, *Surf. Interface Anal.* **15**, 51 (1990).
20. B. Mazurkiewicz and A. Piotrowski, *Corros. Sci.* **23**, 697 (1983).
21. *The Chemistry of the Ferrocyanides*, Vol. 7 in Cyanamid's Nitrogen Chemicals Digest. American Cyanamid Co., NY (1953).
22. T. Drozda and E. Maleczki, *J. Radioanal. Nucl. Chem. Lett.* **95**, 339 (1985).
23. G. P. Halada and C. R. Clayton, *J. Electrochem. Soc.* **138**, 2921 (1991).
24. K. Asami and K. Hashimoto, *Corros. Sci.* **17**, 559 (1977).
25. A. G. Schrott, G. S. Frankel, A. J. Davenport, H. S. Isaacs, C. V. Jahnes and M. Russak, *Surf. Sci.* **250**, 139 (1991).